Frontiers of Information Technology & Electronic Engineering
www.jzus.zju.edu.cn; engineering.cae.cn; www.springerlink.com
ISSN 2095-9184 (print); ISSN 2095-9230 (online)
E-mail: jzus@zju.edu.cn

Integrated 60-GHz miniaturized wideband metasurface antenna in a GIPD process*

Hai-yang XIA[1,2], Jin-can HU[1,2], Tao ZHANG[2,3], Lian-ming LI[†‡1,2], Fu-chun ZHENG[†1,2]
[1]*National Mobile Communications Research Laboratory, Department of Radio Engineering,*
School of Information Science and Engineering, Southeast University, Nanjing 210096, China
[2]*Purple Mountain Laboratories, Nanjing 211111, China*
[3]*School of Microelectronics, Xidian University, Xi'an 710071, China*
[†]E-mail: Lianming.LI@seu.edu.cn; fzheng@ieee.org

Received Aug. 30, 2019; Revision accepted Jan. 5, 2020; Crosschecked Jan. 16, 2020

Abstract: We propose a miniaturized wideband metasurface antenna for 60-GHz antenna-in-package applications. With the glass integrated passive device manufacturing technology, we introduce a coplanar-waveguide-fed (CPW-fed) ring resonator to characterize the material properties of the glass substrate. The proposed antenna is designed on a high dielectric constant glass substrate to achieve antenna miniaturization. Because of the existence of gaps between patch units compared with the conventional rectangular patch in the TM_{10} mode, the radiation aperture of this proposed antenna is reduced. Located right above the center feeding CPW-fed bow-tie slot, the metasurface patch is realized, supporting the TM_{10} mode and antiphase TM_{20} mode simultaneously to improve the bandwidth performance. Using a probe-based antenna measurement setup, the antenna prototype is measured, demonstrating a 10-dB impedance bandwidth from 53.3 to 67 GHz. At 60 GHz, the antenna gain measured is about 5 dBi in the boresight direction with a compact radiation aperture of $0.31\lambda_0\times0.31\lambda_0$ and a thickness of $0.06\lambda_0$.

Key words: 60 GHz; Antenna-in-package (AiP); Coplanar-waveguide-fed (CPW-fed) ring resonators; Glass integrated passive device (GIPD); Metasurface antenna; Miniaturized antenna
https://doi.org/10.1631/FITEE.1900453 **CLC number:** TN82

1 Introduction

Nowadays, many wireless applications such as virtual reality, augmented reality, wireless local area networks, and backhaul must use millimeter-wave (mm-Wave) systems to achieve high data rate and low latency (Ghasempour et al., 2017; da Silva et al., 2018). Accordingly, on top of IEEE 802.11ad, the IEEE 802.11ay standard was defined with new features. Moreover, in mm-Wave bands, the antenna can be integrated into a package using the antenna-in-package (AiP) solution, achieving attractive advantages of high integration levels and small form factors (Zhang and Liu, 2009). Given the current packaging technologies, as the operating frequency and bandwidth of the 60-GHz band are high, it is still challenging to realize low-cost, compact, and high-performance 60-GHz AiP.

Typically, because of their features of low profile, light weight, low cost, and simple planar structure, patch antennas have been widely used in AiP solutions (Wong, 2004). The metasurface technique has been introduced to support the dual modes simultaneously to solve the narrow impedance bandwidth

---

[‡] Corresponding author

[*] Project supported by the National Key R&D Program of China (Nos. 2018YFE0205900 and 2016YFC0800400), the National Science and Technology Major Project, China (No. 2018ZX03001008), and the National Natural Science Foundation of China (Nos. 61306030 and 61674037)

ORCID: Hai-yang XIA, https://orcid.org/0000-0003-0130-7605; Lian-ming LI, https://orcid.org/0000-0003-1873-4806

limitations of the conventional microstrip antenna. In principle, the resonant frequencies of these two modes, which are located on the right-handed (RH) dispersion branch, are close to each other, thereby achieving wide bandwidth (Liu et al., 2015, 2017).

For consumer electronics applications, antenna miniaturization is needed for the mm-Wave system integration. Specifically, for phased-array antennas, with the miniaturized antenna elements, a low mutual coupling can be achieved. A higher-permittivity substrate is preferred to realize antenna miniaturization. Chang et al. (2015) used the glass substrate based on the glass integrated passive device (GIPD) technology to improve the reliability and reduce antenna aperture, fabrication complexity, and cost.

For mm-Wave applications, up to now, several broadside radiation antennas have been realized using the integrated passive device (IPD) technology. Hosono et al. (2016) proposed a 4×4 corporate-feed 70-GHz array antenna with multilayered glass substrate, showing a relative bandwidth of 4% with a gain of 13.5 dBi. Cheng et al. (2018) showed a 2×2 60-GHz circular-polarization antenna array with 13.3% relative bandwidth. A 60-GHz 2×1 array of microstrip-coupled slot antenna was designed on high-resistivity-silicon (HR-silicon) by Biglarbegian et al. (2011), and it achieved a gain higher than 4.95 dBi with more than 11.7% relative bandwidth. A 60-GHz folded dipole antenna and a 60-GHz 1×2 array were designed with a deep cavity, showing relative bandwidths of 12.5% and 5%, respectively (Lantéri et al., 2010). Calvez et al. (2011) introduced a patch antenna with an air cavity, which was excited by a coupling slot in the bipolar complementary metallic-oxide semiconductor (BiCMOS) process. This antenna demonstrated a relative bandwidth of 5% and a simulated gain of 6 dBi. Unfortunately, these antennas suffer from poor performance, large size, and complex structure.

In this study, with the GIPD manufacturing technology, a broadband miniaturized metasurface patch antenna is realized for 60-GHz AiP solutions. A coplanar-waveguide-fed (CPW-fed) ring resonator is implemented to characterize the glass substrate material properties. Because of the high dielectric constant of the glass substrate, the metasurface patch antenna aperture can be reduced. Compared with the conventional rectangular patch in the TM_{10} mode, the existence gaps between the patch units reduce the radiation aperture of this proposed antenna. To expand bandwidth, the metasurface patch supports the TM_{10} mode and antiphase TM_{20} mode simultaneously. With a probe-based antenna measurement setup, the proposed antenna shows an impedance bandwidth from 53.3 to 67 GHz and a gain of about 5 dBi at 60 GHz.

2 AiP prototype topology

Fig. 1 shows the simplified cross-sectional view of the proposed antenna layers. In this design, the main substrate is the D263T thin glass produced by Downdraw Technology, and its thickness is h_1= 300 μm, which is $0.06\lambda_0$ (λ_0 is the wavelength in free space at 60 GHz). In this way, the proposed antenna can achieve the best trade-off between bandwidth and radiation efficiency performances. Two conductive layers M1 and M2, with 5-μm thick electroplated copper, are realized on the substrate surfaces to form the radiation element and its feeding network, respectively. To prevent metal oxidation, both M1 and M2 layers are covered with a PI (polyimide) layer with a dielectric constant of 3.2, a loss tangent of 0.001, and a thickness of h_2=10 μm. With this GIPD process, measurements show that the insertion loss of a 50-Ω CPW line is 0.27 dB/mm at 60 GHz.

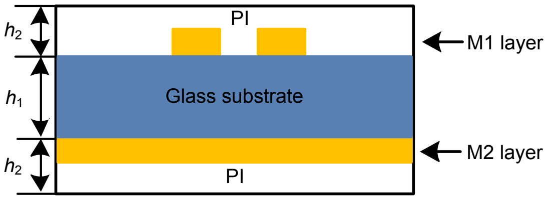

Fig. 1 Simplified cross-sectional view of the antenna layers

Fig. 2 shows the proposed integration scheme of the AiP solution. In this solution, the whole glass substrate can be viewed as an interposer, and both the complementary metallic oxide semiconductor radio frequency (CMOS RF) front-end chip and the main printed circuit board (PCB) are integrated into it. To be specific, the RF chip is soldered on the bottom of the glass substrate with solder balls, while the glass substrate integrated with the RF chip is assembled on the main PCB using a ball grid array. In this study, to evaluate the antenna performance first, only the proposed antenna is fabricated and verified.

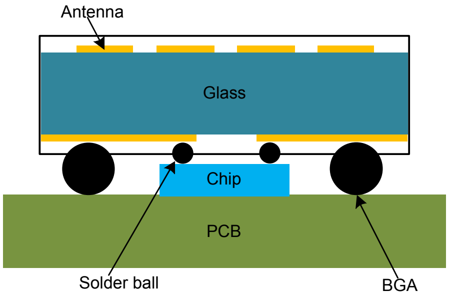

Fig. 2 Proposed integration scheme of the AiP solution (BGA: ball grid array)

3 Electrical properties of materials

For mm-Wave applications, the substrate material property is crucial for accurate antenna design and performance. Typically, most material manufacturers provide only material properties at low frequency, which will decrease the mm-Wave antenna simulation accuracy.

In this work, a ring resonator method is used to extract the material properties of the glass substrate. Fig. 3a shows the top view of the CPW-fed ring resonators layout on the glass substrate (Zou et al., 2002; Thompson et al., 2004). For measurement purposes, the CPW line is used to feed the ring resonator, making it possible to measure the substrate with a 100-µm pitch RF probe. To increase the coupling between the CPW feeding line and the resonator at a lower frequency, a coupler is introduced. At the end of the CPW feeding line, the coupler is a conformal microstrip line, and its corresponding angle φ is 30°. A suitable coupling for the resonators feeding, therefore, can be achieved, balancing the transmission coefficient amplitude at each frequency. With the high-frequency electromagnetic field simulation software (HFSS), the optimized parameters defined in Fig. 3a are shown in Table 1.

Fig. 3b shows the photograph of the fabricated CPW-fed ring resonator on the glass substrate. Fig. 4 shows the measured transmission coefficient of this resonator. The measured data are compared with the simulation results to extract the dielectric constant more accurately. With this method, the permittivity of the glass substrate can be found, matching the measured transmission coefficient well in the end. Fig. 5 summarizes the dielectric constant of the glass substrate. At the 60-GHz band, the extracted substrate effective dielectric constant is 6.47. Note that due to measurement errors and fabrication tolerance, the precision of the extracted permittivity is about ±0.05.

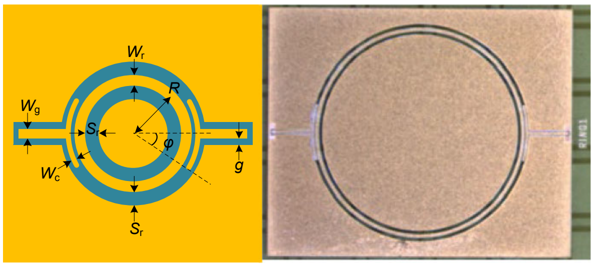

(a) (b)

Fig. 3 Layout of the CPW-fed ring resonator on the glass substrate for ground-signal-ground (GSG) probe testing (a) and photograph of the fabricated CPW-fed ring resonator (b)

Table 1 Optimized parameters of the CPW-fed ring resonator

Parameter	Value (mm)	Parameter	Value (mm)
W_g	0.07	S_r	0.10
g	0.025	W_c	0.05
R	1.535	W_r	0.07

4 Antenna design

Fig. 6 shows the geometry of the proposed metasurface antenna. The antenna aperture is on the M1 layer and consists of 2×2 square patch units. With the benefit of the glass substrate high dielectric constant feature, a miniaturized size ($0.31\lambda_0 \times 0.31\lambda_0$) of the antenna can be achieved. Compared with the free-space wavelength, the pitch of the square patch unit p is small, and the 2×2 square patch unit can be regarded as a two-dimensional finite periodic structure. The M2 layer acts as a ground plane, and a CPW-fed bow-tie slot is implemented on it. For the antenna's proper excitation, the slot is located at the upper metasurface center. The slot length (s_l) determines the resonant frequency; with a narrower slot width and a wider extended angle θ, the bandwidth performance can be improved (Huang and Kuo, 1998;

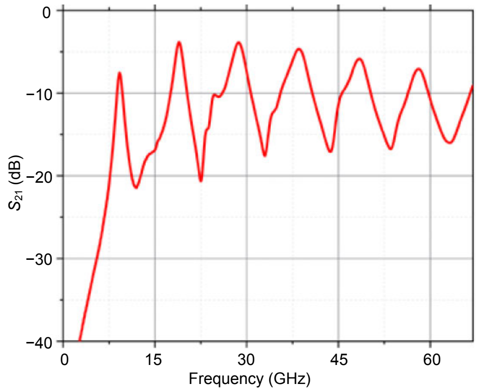

Fig. 4 Measured S_{21} of the CPW-fed ring resonator

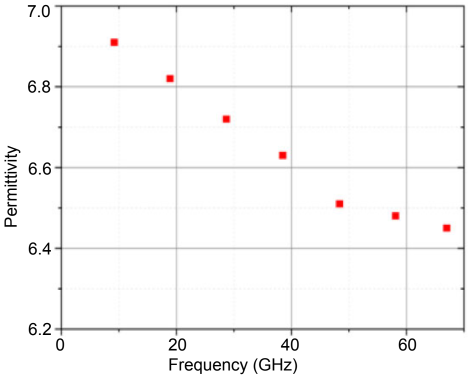

Fig. 5 Dielectric constant of the glass substrate

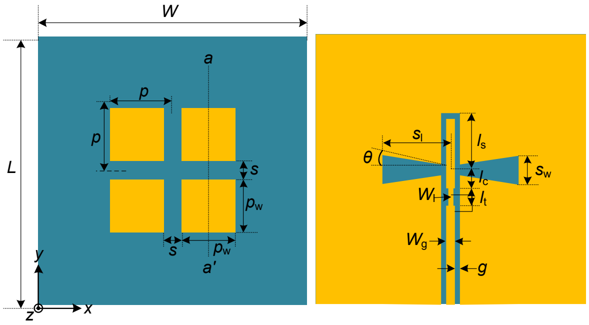

(a) (b)

Fig. 6 Geometry of the proposed metasurface antenna: (a) top view; (b) bottom view

Tavakol et al., 2010). To achieve broadband impedance matching, both an open stub and a high impedance line are added, providing capacitance and inductance effects, respectively.

In this design, with the low profile of the glass substrate, a transmission line model is used to analyze the proposed metasurface antenna. Due to the fringing field, the patch antenna's electrical dimension is greater than its physical dimension. The extended length ΔL at each patch end can be given by (Balanis, 2016)

$$\frac{\Delta L}{h_1}=\frac{0.412(\varepsilon_{\mathrm{reff}}+0.3)\left(\dfrac{W_{\mathrm{p}}}{h_1}+0.262\right)}{(\varepsilon_{\mathrm{reff}}-0.258)\left(\dfrac{W_{\mathrm{p}}}{h_1}+0.813\right)}. \tag{1}$$

The antenna's effective dielectric constant $\varepsilon_{\mathrm{reff}}$ and width W_{p} are defined as follows:

$$\varepsilon_{\mathrm{reff}}=\frac{\varepsilon_{\mathrm{r}}+1}{2}+\frac{\varepsilon_{\mathrm{r}}-1}{2}\left(1+12\frac{h_1}{W_{\mathrm{p}}}\right)^{-1/2}, \tag{2}$$

$$W_{\mathrm{p}}=2p-s, \tag{3}$$

where s is the spacing of the square patch unit. Note that the physical size of the patch unit p_{w} equals $p-s$. In the effectively extended region with a length of ΔL at each end, the propagation constant along the resonant direction is given by

$$\beta_{\mathrm{eff}}=\frac{2\pi f}{c}\sqrt{\varepsilon_{\mathrm{reff}}}, \tag{4}$$

where f is the operating frequency, c the light speed in the vacuum, and β_{eff} the propagation constant in the fringing field.

Fig. 7 shows the patch unit simulation model for the dispersion relation extraction. With the simulated S-parameters, the propagation constant of the patch unit β_{u} is extracted with the following function:

$$\beta_{\mathrm{u}}=\arccos\left(\frac{1-S_{11}S_{22}+S_{12}S_{21}}{2S_{21}}\right), \tag{5}$$

where S_{11} is the input reflection coefficient, S_{21} the forward transmission coefficient, S_{22} the output reflection coefficient, and S_{12} the reverse transmission coefficient.

In this design, the TM_{10} mode and antiphase TM_{20} mode are introduced in the metasurface antenna. These two resonant modes are close to each other in the RH dispersion branch to improve the impedance bandwidth. To illustrate the operation principle of the TM_{10} resonant mode, Fig. 8 shows the simulated electric field distribution of the TM_{10} mode. In this mode, the E-field distribution of the 2×2 square patch units is similar to the mode of the rectangular microstrip patch. It is found that compared to the traditional patch antenna, given the existence gaps between patch units, the overall physical size of this proposed antenna is reduced.

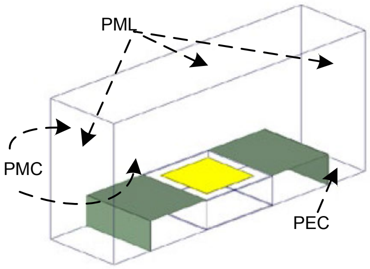

Fig. 7 Patch unit simulation model for the dispersion relation extraction

PMC: perfect magnetic conductor; PML: perfectly matched layer; PEC: perfect electrical conductor

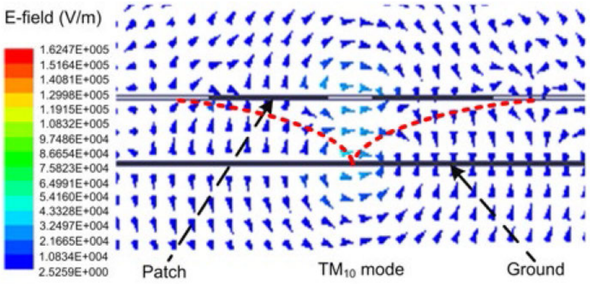

Fig. 8 Simulated electric field distribution of the TM_{10} mode (*aa′* plane, *x*=0.445 mm, 59.5 GHz)

To meet the TM_{10} mode resonant conditions, the sum of the twice-patch unit pitch $2p$ and the extended length ΔL at the antenna end equals half the wavelength of the operating frequency. It follows that

$$2\beta_{\mathrm{u}}p+2\beta_{\mathrm{eff}}\Delta L=\pi. \tag{6}$$

Fig. 9 shows the simulated electric field distribution of the antiphase TM_{20} mode. In this mode, the gap between the patch units is also used to change the E-field distribution. Notably, the directions of the E-field at the opposite sides of the central gap region are antiparallel. Hence, with the help of the TM_{10} and TM_{20} modes, the broadside radiation pattern can be achieved.

To meet the antiphase TM_{20} mode resonant conditions, the sum of the single patch unit pitch p and its extended length ΔL is about half the wavelength. Based on this field distribution, the function of the antiphase mode is given by

$$\beta_{\mathrm{u}}p+2\beta_{\mathrm{eff}}\Delta L=\pi. \tag{7}$$

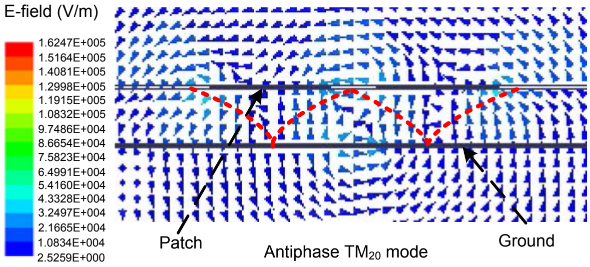

Fig. 9 Simulated electric field distribution of the antiphase TM_{20} mode (*aa′* plane, *x*=0.445 mm, 63 GHz)

With the simulation model in Fig. 7, the dispersion relation of the patch unit is plotted (Fig. 10). Notably, the resonant frequencies of these two modes are 59.5 and 63.0 GHz, corresponding to the TM_{10} and antiphase TM_{20} modes, respectively. With HFSS, the optimized values of the proposed metasurface antenna parameters defined in Fig. 6 are shown in Table 2.

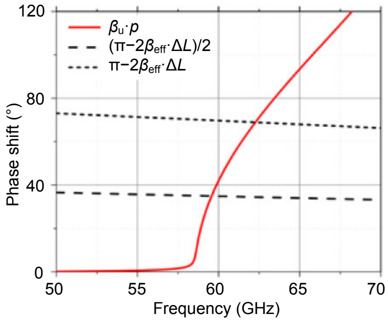

Fig. 10 Dispersion diagram of the patch unit model

5 Measurement results

Fabricated with GIPD technology, Fig. 11 shows the photograph of the proposed antenna prototype. The on-wafer measurement is undertaken by Cascade

Microtech 67-GHz GSG RF probes with a 100-μm pitch.

The antenna S-parameters are measured with the probe station. The proposed antenna is fixed on the foam above the metal carrier, and the foam material has a height of about 10 mm, which is twice the wavelength at 60 GHz. Fig. 12 shows the simulated and measured return loss of the metasurface patch antenna. Notably, the 10-dB impedance bandwidth is between 53.3 and 67 GHz (limited by the measurement instruments). The discrepancy between the measured and simulated results is attributed to the fabrication tolerance, measurement error, and other uncertainties. Furthermore, for the S-parameter measurement, due to the energy reflected by the metal carrier, a resonant mode is introduced around 58 GHz.

For the far-field performance measurement, a probe-based antenna measurement setup in an anechoic chamber is used (Fig. 13). In this measurement, to relax the effect of the RF probe on the antenna radiation pattern, the RF probe is covered with an absorbing material. With the probe station, the test sample is fixed on a foam material AUT (antenna under test) sample holder, which has a similar permittivity to the air. Fig. 14 presents the simulated and measured gains of the metasurface patch antenna in the broadside direction. Notably, the measurement

Table 2 Optimized parameters of the proposed antenna

Parameter	Value (mm)	Parameter	Value (mm)
W	5.00	l_t	0.40
L	5.00	s_l	0.65
p	0.89	s_w	0.30
p_w	0.64	W_l	0.03
s	0.25	W_g	0.06
l_s	0.65	g	0.025
l_c	0.15		

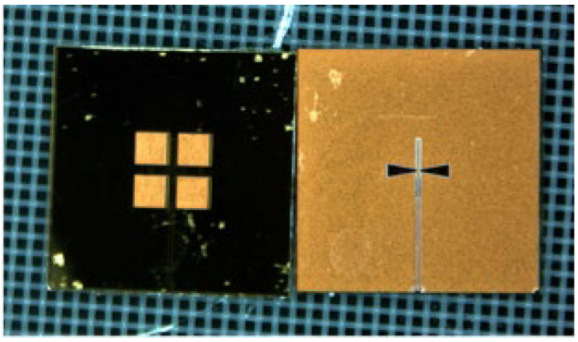
(a) (b)

Fig. 11 Fabricated antenna prototype: (a) top view; (b) bottom view

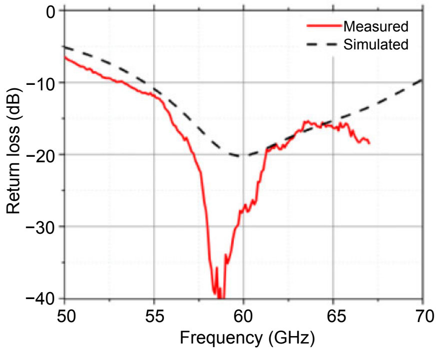

Fig. 12 Simulated and measured reflection coefficients of the proposed antenna

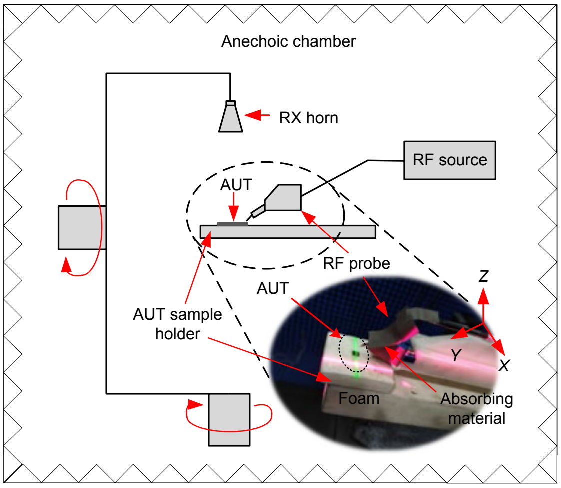

Fig. 13 Probe-based antenna measurement setup in an anechoic chamber for far-field performance measurement

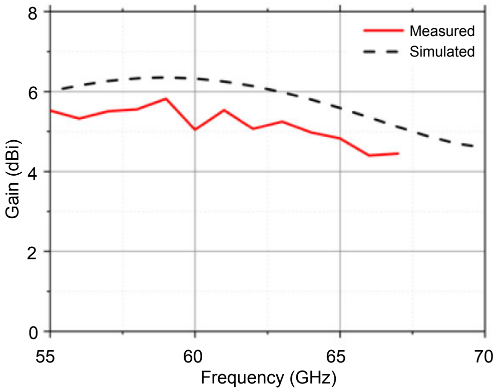

Fig. 14 Simulated and measured gains of the proposed antenna

results agree well with the simulation results. In particular, the gain is higher than 4.5 dBi from 57 to 66 GHz, with a peak gain of 5.5 dBi at 59 GHz.

For performance comparison, Table 3 summarizes the performance of the proposed antenna and those in previous works. As indicated, with the GIPD process, the proposed metasurface antenna structure has a compact radiation aperture size and achieves wide bandwidth performance.

Figs. 15 and 16 present the E- and H-plane radiation patterns at 60 GHz, respectively. Note that the E-plane cannot be measured within the whole angular range, as it is blocked by some parts of the measurement assembly. The 3-dB beam widths in the E- and H-plane are 43° and 64°, respectively. Good simulation to measurement correlation is achieved in both the E- and H-plane. Due to reflections by the probe station, there exist some ripples in the radiation pattern. In the E-plane, because of the metal cable reflections, the measured back lobe is greater than the simulation results.

6 Conclusions

In this paper, a miniaturized wideband metasurface antenna has been proposed for 60 GHz applications. With GIPD manufacturing technology, the antenna was designed on a high dielectric constant glass substrate, and the $0.31\lambda_0 \times 0.31\lambda_0$ radiation aperture has been realized. To expand bandwidth, with a CPW-fed bow-tie slot on the ground plane, the metasurface patch supported the TM_{10} mode and antiphase TM_{20} mode simultaneously. Based on the probe-based antenna measurement setup, the proposed antenna showed a wide impedance bandwidth from 53.3 to 67 GHz. The measured gain of the antenna was above 4.5 dBi from 57 to 66 GHz with a low profile of $0.06\lambda_0$ at 60 GHz.

Contributors

Hai-yang XIA designed the research. Hai-yang XIA and Jin-can HU processed the data. Hai-yang XIA wrote the first draft of the manuscript. Tao ZHANG and Lian-ming LI helped

Table 3 Comparison between the proposed antenna and those in previous works

Reference	Type	f_0 (GHz)/FBW	Gain (dBi)	Radiation aperture (width×length)	Thickness	Technology
Hosono et al. (2016)	4×4 corporate-feed array antenna	70/4%	13.5	N/A	$0.187\lambda_0$	Multi-layered GIPD
Cheng et al. (2018)	2×2 circular-polarization antenna array	60/>13.3%	N/A	N/A	N/A	GIPD
Biglarbegian et al. (2011)	2×1 array of microstrip-coupled slot antenna	60/11.7%	4.95	$0.4\lambda_0 \times 0.9\lambda_0$	$0.056\lambda_0$	HR-silicon IPD
Lantéri et al. (2010)	Folded dipole antenna 1×2 folded dipole array	60/12.5% 60/5%	7 8	N/A	N/A	GIPD with deep cavity
Calvez et al. (2011)	Patch antenna	60/5%	5*	$0.33\lambda_0 \times 0.33\lambda_0$	$0.06\lambda_0$	GIPD with air cavity
This work	Metasurface patch antenna	60/>22.8%	5.5	$0.31\lambda_0 \times 0.31\lambda_0$	$0.06\lambda_0$	GIPD

* Simulation results. FBW: fractional bandwidth. N/A: not applicable

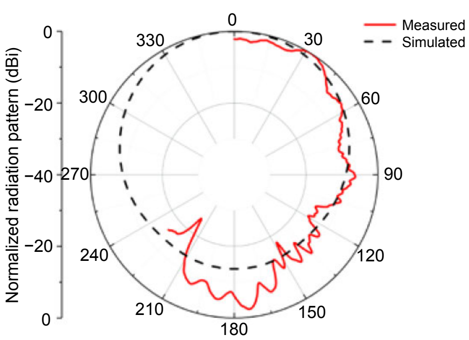

Fig. 15 Simulated and measured normalized radiation patterns of the proposed antenna at 60 GHz in the E-plane

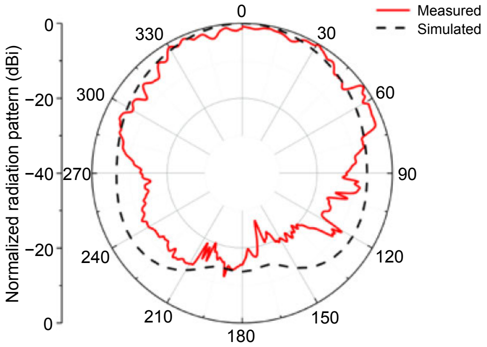

Fig. 16 Simulated and measured normalized radiation patterns of the proposed antenna at 60 GHz in the H-plane

organize the manuscript. Hai-yang XIA, Lian-ming LI, and Fu-chun ZHENG revised and edited the final version.

Compliance with ethics guidelines

Hai-yang XIA, Jin-can HU, Tao ZHANG, Lian-ming LI, and Fu-chun ZHENG declare that they have no conflict of interest.

References

Balanis CA, 2016. Antenna Theory: Analysis and Design. John Wiley & Sons, Hoboken.

Biglarbegian B, Nezhad-Ahmadi MR, Safavi-Naeini S, 2011. Integrated microstrip-fed slot array antenna for emerging wireless application in IPD technology. Proc IEEE MTT-S Int Microwave Workshop Series on Millimeter Wave Integration Technologies, p.41-44. https://doi.org/10.1109/IMWS3.2011.6061882

Calvez C, Person C, Coupez JP, et al., 2011. Miniaturized hybrid antenna combining Si and IPD™ technologies for 60 GHz WLAN applications. Proc IEEE Int Symp on Antennas and Propagation, p.1357-1359. https://doi.org/10.1109/APS.2011.5996542

Chang CC, Lin CC, Cheng WK, 2015. Fully integrated 60 GHz switched-beam phased antenna array in glass-IPD technology. *Electron Lett*, 51(11):804-806. https://doi.org/10.1049/el.2015.0891

Cheng WK, Chang CC, Tsai TH, 2018. Design of 60 GHz circular-polarization antenna array in glass-IPD for monostatic radar MMICs. Proc IEEE Int Symp on Radio-Frequency Integration Technology, p.1-3. https://doi.org/10.1109/RFIT.2018.8524028

da Silva CRCM, Kosloff J, Chen C, et al., 2018. Beamforming training for IEEE 802.11ay millimeter wave systems. Proc Information Theory and Applications Workshop, p.1-9. https://doi.org/10.1109/ITA.2018.8503112

Ghasempour Y, da Silva CRCM, Cordeiro C, et al., 2017. IEEE 802.11ay: next-generation 60 GHz communication for 100 Gb/s Wi-Fi. *IEEE Commun Mag*, 55(12):186-192. https://doi.org/10.1109/MCOM.2017.1700393

Hosono R, Uemichi Y, Nukaga O, et al., 2016. 70-GHz band corporate-feed array antenna with multi-layered glass substrate. Proc IEEE Int Symp on Antennas and Propagation, p.799-800. https://doi.org/10.1109/APS.2016.7696108

Huang JF, Kuo CW, 1998. CPW-fed bow-tie slot antenna. *Microw Opt Technol Lett*, 19(5):358-360. https://doi.org/10.1002/(SICI)1098-2760(19981205)19:5<358::AID-MOP14>3.0.CO;2-X

Lantéri J, Dussopt L, Pilard R, et al., 2010. 60 GHz antennas in HTCC and glass technology. Proc the 4th European Conf on Antennas and Propagation, p.1-4.

Liu W, Chen ZN, Qing XM, 2015. Metamaterial-based low-profile broadband aperture-coupled grid-slotted patch antenna. *IEEE Trans Antenn Propag*, 63(7):3325-3329. https://doi.org/10.1109/TAP.2015.2429741

Liu W, Chen ZN, Qing XM, et al., 2017. Miniaturized wideband metasurface antennas. *IEEE Trans Antenn Propag*, 65(12):7345-7349. https://doi.org/10.1109/TAP.2017.2761550

Tavakol V, Qi F, Ocket I, et al., 2010. CPW-fed slot bow-tie antenna at 90 GHz for a mm-wave detector matrix. Proc 4th European Conf on Antennas and Propagation, p.1-3.

Thompson DC, Tantot O, Jallageas H, et al., 2004. Characterization of liquid crystal polymer (LCP) material and transmission lines on LCP substrates from 30 to 110 GHz. *IEEE Trans Microw Theory Techn*, 52(4):1343-1352. https://doi.org/10.1109/TMTT.2004.825738

Wong KL, 2004. Compact and Broadband Microstrip Antennas. John Wiley & Sons, New York.

Zhang YP, Liu DX, 2009. Antenna-on-chip and antenna-in-package solutions to highly integrated millimeter-wave devices for wireless communications. *IEEE Trans Antenn Propag*, 57(10):2830-2841. https://doi.org/10.1109/TAP.2009.2029295

Zou G, Gronqvist H, Starsk JP, et al., 2002. Characterization of liquid crystal polymer for high frequency system-in-a-package applications. *IEEE Trans Adv Packag*, 25(4): 503-508. https://doi.org/10.1109/TADVP.2002.807593